



Passive superresolution imaging of incoherent objects

JERNEJ FRANK,  ALEXANDER DUPLINSKIY, KADEN BEARNE, AND A. I. LVOVSKY*

Department of Physics, University of Oxford, Oxford OX1 3PU, UK

*alex.lvovsky@physics.ox.ac.uk

Received 20 April 2023; revised 25 July 2023; accepted 30 July 2023; published 22 August 2023

The need to observe objects that are smaller than the diffraction limit has led to the development of various superresolution techniques. However, most such techniques require active interaction with the sample, which may not be possible in multiple practical scenarios. The recently developed technique of Hermite–Gaussian imaging (HGI) achieves superresolution by passively observing the light coming from an object. This approach involves decomposing the incoming field into the Hermite–Gaussian basis of spatial modes and measuring the amplitude or intensity of each component. From these measurements, the original object can be reconstructed. However, implementing HGI experimentally has proven to be challenging, and previous achievements have focused on coherent imaging or parameter estimation of simple objects. In this paper, we implement interferometric HGI in the incoherent regime and demonstrate a three-fold improvement in the resolution compared to direct imaging. We evaluate the performance of our method under different noise levels. Our results constitute a step towards powerful passive superresolution imaging techniques in fluorescent microscopy and astronomy.

Published by Optica Publishing Group under the terms of the [Creative Commons Attribution 4.0 License](https://creativecommons.org/licenses/by/4.0/). Further distribution of this work must maintain attribution to the author(s) and the published article's title, journal citation, and DOI.

<https://doi.org/10.1364/OPTICA.493718>

1. INTRODUCTION

With the human eye, we can see only objects as small as a thin strand of hair, which is about 100 μm in width [1]. Modern life and materials sciences are keen to study structures well beyond this limit, and microscopy is an indispensable tool for this purpose. The resolution of conventional optical microscopy is, however, limited due to diffraction on the objective lens to approximately half of the optical wavelength ($\sim 200\text{ nm}$) [2–4]. In the last few decades, superresolution (SR) imaging techniques emerged focusing on either manipulating the illumination of the sample or using stochastic properties of fluorescent emitters to achieve resolution well beyond the diffraction limit [5–8]. Some of these methods were marked by the 2014 Nobel Prize in Chemistry [9]. Even higher resolution—down to single nanometers—can be achieved by atomic force microscopy [10] and electron microscopy [11]. However, all existing SR methods involve active interaction with the sample, which imposes significant limitations. First, they involve the risk of altering or damaging the samples. Second, these techniques are not universally applicable to all imaging scenarios since they rely on specific underlying properties of the samples, such as, e.g., nonlinear susceptibility. Even if the sample is amenable to a particular method, SR microscopes require expert knowledge, and various parameters must be adjusted on a case-by-case basis to render a truthful image reconstruction.

These limitations can be overcome if the imaging method involves only *far-field*, *linear-optical*, and *passive measurement of the optical field arriving from the object*. In 2016, Tsang *et al.* [12–16]

theoretically predicted that the diffraction limit can be overcome for estimating the distance between two incoherent point sources in the far-field regime by decomposing the field in the image plane into an orthonormal basis of spatial modes [typically, Hermite–Gaussian (HG)] and measuring the intensity of each component. This approach, dubbed SpaDe for “spatial demultiplexing,” was soon experimentally demonstrated by various groups [17–23].

On this basis, Yang *et al.* proposed an extension into reconstructing complete 2D objects dubbed HG imaging (HGI) [17]. Pushkina *et al.* experimentally implemented HGI for coherent 2D objects and showed a two-fold resolution improvement over the diffraction limit [24].

However, the latter experimental work used coherent light to illuminate the sample and detect the reflected light. On the other hand, fluorescence emitted by biological samples is incoherent. Also, if SpaDe is to be applied outside microscopy, say, in astronomy or remote imaging, it needs to be adapted to incoherent input. Here we address this requirement by extending HGI to imaging incoherent 2D objects. Since the incoherent light emitted from the object lacks phase information, it is necessary to measure in an overcomplete spatial mode basis, involving not only HG modes but also their superpositions. We measure the intensity in each basis mode using heterodyne detection and then utilize a deep neural network (DNN) to reconstruct the objects. We observe a significant resolution improvement over direct imaging (DI) in various scenarios and certified by quantitative benchmarks.

2. THEORETICAL BACKGROUND

A. Image Reconstruction Theory

We briefly recap the reconstruction method of Yang *et al.* [17]. The object being imaged is defined by the incoherent intensity distribution $I(x, y)$. We reconstruct this distribution by expanding it into the HG basis

$$I_{\text{rec}}(x, y) = \sum_{m,n=0}^N \frac{\beta_{mn} \phi_{mn}(x, y)}{2^{m+n+2} m! n! \pi \sigma^2}, \quad (1)$$

where $\phi_{mn}(x, y) = H_m(\frac{x}{\sqrt{2}\sigma}) H_n(\frac{y}{\sqrt{2}\sigma}) e^{-\frac{x^2+y^2}{4\sigma^2}}$ are HG polynomials, N is the cutoff for the number of HG modes to be used, $\sigma \approx 0.21\lambda/\text{NA}$ is the radius of the PSF at $e^{-1/2}$ intensity [25], and β_{mn} are expansion coefficients. The point spread function (PSF) mode is assumed to match ϕ_{00} .

These coefficients can be obtained experimentally by measuring the powers of the heterodyne detector photocurrents with the local oscillator (LO) prepared in a set of modes (see Supplement 1 for a full derivation). This set of modes can be the HG basis [Fig. 1(a)]; however, in this case, we are able to recover only the β 's with even indices, which, in turn, allow us to reconstruct only the even component of the object intensity distribution: $I_{\text{even}}(x, y) = [I(x, y) + (-x, y) + I(x, -y) + I(-x, -y)]/4$, which results in ghost image artifacts [13,17]. To address this problem, Yang *et al.* [17] proposed displacing the object into a single quadrant of the x - y plane, thereby separating the image from its "ghosts." However, the displaced object together with the ghosts is larger in size and requires higher-order modes for its expansion into the HG basis. Furthermore, this approach is unsuitable for objects with a wide spatial extent.

Tsang *et al.* proposed an alternative strategy: recovering the odd components of the image by measuring the powers in an overcomplete mode basis known as interferometric HG (iHG) [13,26]. The version of the iHG basis used in our work includes the following superpositions of individual HG modes [Fig. 1(b)]:

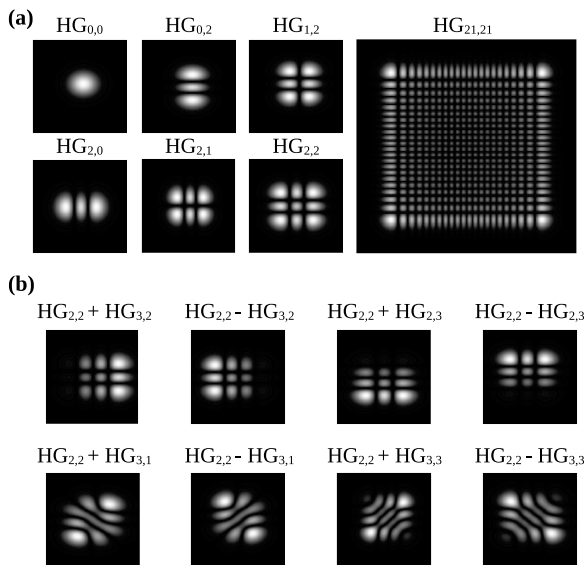


Fig. 1. (a) Subset of holograms displayed on the spatial light modulator (SLM) to generate the LO in Hermite–Gaussian modes. (b) Expanded iHG basis, which includes eight additional superpositions of neighboring HG modes to obtain the odd geometric moments for image reconstruction.

$$\phi_{mn}^{0-8} := \{\phi_{mn}, \phi_{m,m+1,n,n}^{\pm}, \phi_{m,m,n,n+1}^{\pm}, \phi_{m,m+1,n,n+1}^{\pm}, \phi_{m,m+1,n,n-1}^{\pm}\},$$

where

$$\phi_{m,m',n,n'}^{\pm} := \frac{1}{\sqrt{2}} [\phi_{m'n'} \pm \phi_{mn}]. \quad (2)$$

For each mode ϕ_{mn}^i , the power P_{mn}^i of the associated heterodyne photocurrent is measured. These measurements then evaluate the coefficients β_{mn} , from which the image is recovered (see Supplement 1). Note that theoretically, iHG modes ϕ_{mn}^i with $i \in \{0, \dots, 6\}$ are sufficient for complete reconstruction. However, the experiment uses the entire iHG mode set with $i \in \{0, \dots, 8\}$, as defined above.

B. Simulations

To test the viability of our approach, we first simulate image reconstruction computationally using Eq. (1) and compare it to simulated DI. We set the numerical aperture (NA) to 5.5×10^{-4} and $\lambda = 785$ nm (the same as used in the experiment).

As our objects, we use symbols of a bitmap ASCII font. Each symbol is a black-and-white bitmap 8×6 pixels, with the size of each pixel being 0.36σ [Fig. 2(a), upper left panel]. To simulate DI, we convolve the PSF with the objects [Fig. 2(a), upper middle panel]. The upper right panel of Fig. 2(a) shows the result of applying the conventional Richardson–Lucy (RL) deconvolution algorithm [27] to the DI data. Next, we simulate the image reconstruction for various cutoff numbers $N = 2, 5, 30$ [Fig. 2(a), bottom row]. As can be seen, the DI of most of the letters is unreadable, whether or not RL is applied. But HGI allows us to achieve a satisfactory level of readability, the quality improving with N .

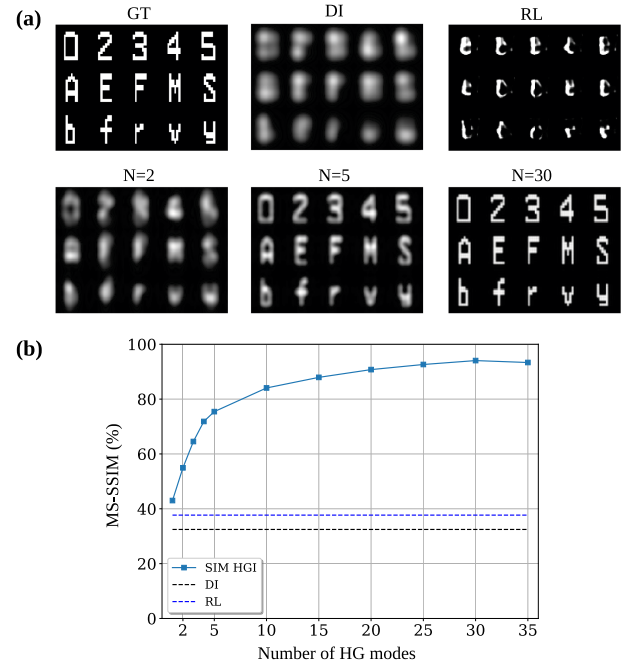


Fig. 2. (a) Letters of the alphabet with varying resolution. Top row: GT is the ground truth, DI represents the direct image whose resolution is limited by diffraction, and RL is the Richardson–Lucy deconvolution of the DI. Bottom row: simulated HGI reconstructions in an idealized setting with up to $m = n = N = 2, 5, 30$ modes. (b) MS-SSIM calculated between (1) ground truth (infinite resolution) and (2) simulated HGI, DI, and RL reconstructions. MS-SSIM score of $\geq 80\%$ achieves letter readability.

We quantify the image quality with respect to the ground truth objects by computing multi-scale structural similarity (MS-SSIM) [28] [Fig. 2(b)], which is a popular metric in the image processing community, designed to mimic how the human eye perceives images [29]. We find that the resolution improvement is proportional to N and saturates for $N > 25$. Comparing the images with the MS-SSIM graph in Fig. 2, we can see that satisfactory image quality is achieved at about 80%.

3. EXPERIMENT

A. Setup

We adopt the experimental setup from Ref. [24] (Fig. 3). We use a continuous wave diode laser (Eagleyard EYP-DFB-0785), operating at 785 nm. The powers of the image field in individual HG modes are measured by means of heterodyne detection with the LO prepared in the corresponding mode.

At the outset, we split the laser into the signal LO paths. We use the signal path to illuminate the object displayed on a digital micromirror device (DMD) (DLP LightCrafter 6500). The DMD pixel pitch is 7.56 μm , and our objects are displayed in a square area of 160×160 pixels. This area is divided into 10×10 “logical pixels,” each being a square of 16×16 physical DMD pixels. Our binary objects are bitmaps of these logical pixels. To simulate incoherent objects, the DMD displays logical pixels one at a time, and for each pixel, photocurrent powers P_{mn}^i for all iHG modes are measured. To determine P_{mn}^i corresponding to a given multi-pixel object, we digitally add the measured values of P_{mn}^i for all of the object’s pixels. This approach is chosen instead of the usual method of obtaining spatial incoherence via a rotating ground glass because the latter method would require averaging of the speckle pattern for each object and each combination (m, n, i) , resulting in prohibitively slow data acquisition.

After light is reflected from the object, we collect it by an objective lens. In front of the objective lens, at a distance 242.5 cm away from the DMD, we place an iris of diameter 2.66 mm to reduce the NA to 5.5×10^{-4} . This configuration sets the Rayleigh diffraction limit to a spacing of seven logical DMD pixels (870 μm).

To generate a particular iHG mode in the LO path, we display a phase grating (“hologram”) on a reflective phase-only liquid-crystal-on-silicon SLM (Hamamatsu X13138-02) and select the first diffraction order of the reflected light [30,31]. We switch through holograms corresponding to different iHG modes sequentially.

The signal and LO are recombined on a beam splitter and sent onto a balanced detector. By placing a flip mirror after the objective

lens, we are able to switch between recording HGI with the heterodyne detector and DI using a high-resolution CMOS camera.

B. Deep Neural Networks

As realized in Ref. [24], experimental imperfections such as an imperfect Gaussian PSF, optical aberrations, shot noise, electronic white noise, optical misalignment, iHG mode fidelity in the LO, imperfect overlap between signal and LO, and general air fluctuation or vibrations render an image reconstruction using Eq. (1) impossible because the measurement errors of lower-order iHG modes propagate into higher-order β_{mn} coefficients.

We, therefore, recast our reconstruction problem into a machine-learning task and let a DNN find an optimal mapping between imperfect measurements and the underlying basis needed for image reconstruction. In this way, we can benefit from both the new physics of HGI measurement and machine learning to extract the image with the highest possible resolution. The neural network takes the measured photocurrent powers as input and outputs the reconstructed image.

The DNN architecture is shown in Fig. 4(a). We have four fully connected hidden layers with 400-800-800-400 neurons. The activation functions are hyperbolic tangent in the first layer and rectified linear unit (ReLU) in the next three layers; the last layer adapts the $[0, 1]$ range by using sigmoid.

To acquire the DNN training and cross-validation sets, we obtain the photocurrent powers in iHG modes ϕ_{mn}^l , with $m, n \in \{0, \dots, 20\}$ and $l \in \{0, \dots, 8\}$ for 20,000 bitmaps representing random matrices, ellipses, and lines [Fig. 4(b)]. To investigate the dependence of reconstruction quality on the number of modes acquired, several subsets are selected from the above set, corresponding to $m, n \leq M$, with $M = 1, 4, 9, 14, 20$. These subsets are split into training and cross-validation sets in proportion 90:10.

Using the ground truth images for labels would lead to severe overfitting [24]—so the DNN is trained to model the training set too precisely and therefore fails to generalize to previously unknown inputs. We, therefore, produce our labels according to Eq. (1). That is, our label is the image of the object as if it were

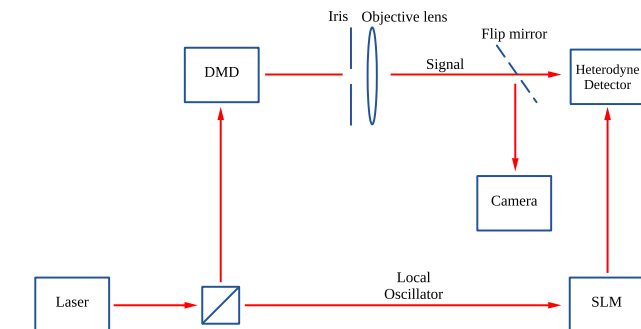


Fig. 3. Experimental setup to image incoherent objects with HGI via homodyne detection and DI.

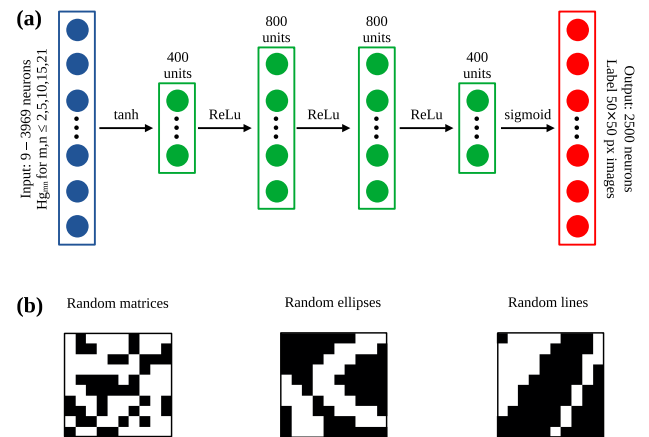


Fig. 4. (a) Architecture of the DNN used for image reconstruction from iHG modes. The input layer (blue) dimension varies with the number of iHG modes utilized. The hidden layers (green) reduce the latent space to 400 neurons. The output layer (red) is fixed to output images 50×50 pixels. (b) Examples of bitmaps used for training the DNN.

reconstructed via HGI in the absence of imperfections. We produced several label sets of varied resolution by choosing the mode cutoff number N between five and 35.

For DNN training, we set our loss function to be the mean squared error (MSE) and use a minibatch size of 32. We use the adaptive moment estimation (Adam) optimizer, learning rate 10^{-4} , exponential moving averaging parameters for the first and second moment estimates (0.9, 0.999), respectively, and weight decay zero. The training is run on an 11th Generation Intel Core i9-11900K CPU with 64 GB memory and an NVIDIA RTX A5000 GPU with 24 GB memory. Training the DNN up to 2000 epochs takes 40–60 min on average.

4. RESULTS

We evaluate the performance of our method in two ways: (1) we look at qualitative image reconstruction of the object as a whole using alphabet letters [Fig. 2(a)]; (2) we measure the resolution of the system using the Rayleigh criterion with pairs of parallel lines of varied separation. None of the objects used for performance evaluation belongs to the training set. The experimental data for these objects have been acquired separately from the training set data.

We train several DNNs where we vary both the number M of iHG modes in the input and the number N of HG modes used in simulating the labels. To show that the resolution improvement arises due to the new physics of HGI measurements and not only due to machine learning, we also trained the same DNN using DI intensity measurements as inputs. These inputs are $63 \times 63 = 3969$ pixel bitmaps that correspond to roughly the same dimension of the input layer as for iHG with $M = 20$.

We compare the results qualitatively by looking at the image reconstruction results [Fig. 5(a)] and quantitatively by computing the MS-SSIM between the ground truth (infinite resolution) and the respective outputs of the DNNs [Fig. 5(c)].

We see that the resolution improvement is maximized for $N = 30$ label modes and $M = 10$ to 15 measured iHG modes.

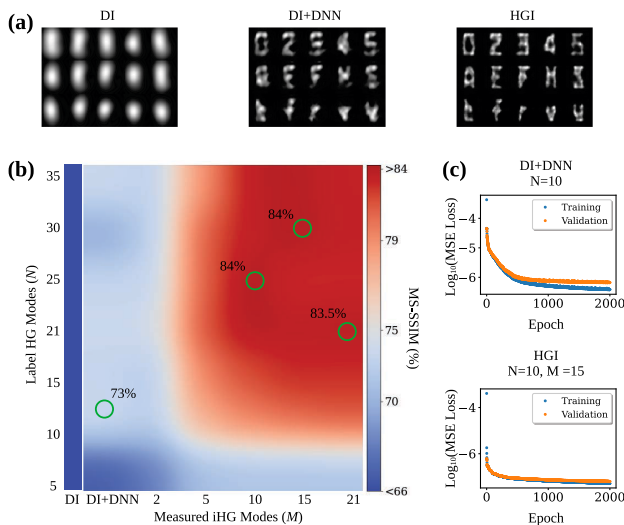


Fig. 5. (a) Alphabet letters imaged using DI (left), DNN-enhanced DI (middle), and HGI using $M = 15$ iHG modes (right). (b) Multi-scale structural similarity values for different pairs of input and label mode numbers. (c) Training and cross-validation MSE as a function of training epoch. DI+DNN overfits, and we stop training at 1000 epochs, while for HGI, we train for the complete 2000 epochs.

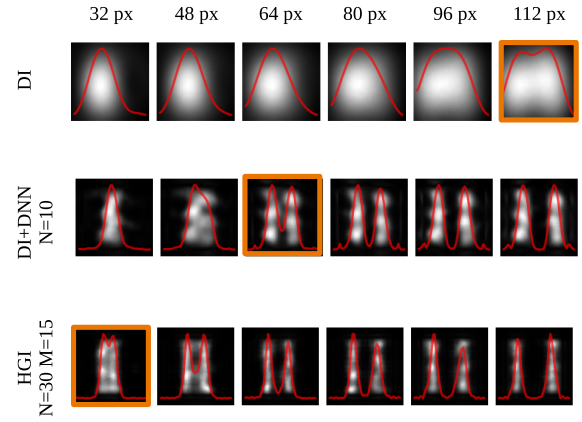


Fig. 6. Reconstructed images of pairs of parallel lines via direct imaging (top), DNN-enhanced direct imaging (middle), and HGI (bottom). Colored frames correspond to the resolution limits in the three settings.

We attribute the lack of resolution improvement for higher M to the photocurrents in higher-order iHG modes being very low and hence prone to noise.

We can also observe some resolution improvement beyond the diffraction limit with DI purely through DNN software enhancement. However, this enhancement is smaller than that of HGI. We can see this directly from the reconstructed images [Fig. 5(a)] and from the MS-SSIM benchmarks [Fig. 5(b)]. We also observe that training the DNN for DI with the number N of label modes as low as 10 quickly leads to overfitting, which reduces the reconstruction quality on the test set [Fig. 5(c)].

To determine the resolution limit, we reconstruct the images for pairs of parallel lines and measure the intensity profile by integrating over the vertical dimension [Fig. 6]. We see that the resolution of DI is limited by the diffraction limit, corresponding to a line separation of seven logical DMD pixels ($847 \mu\text{m}$). DI+DNN gives some improvement over that limit by resolving lines four logical pixels ($484 \mu\text{m}$) apart, but HGI is able to resolve the separation of two logical pixels ($242 \mu\text{m}$). Compared to DI and DI+DNN, this corresponds to, respectively, a ~ 3 -fold and ~ 2 -fold resolution enhancement.

Last, we investigate the effect of simulated shot noise on the performance of HGI and DI. To this end, we assume that all measurements (iHG mode intensities in HGI and pixel intensities in DI) are implemented via photon counting, and the total number of photons detected is N_{ph} . Then the number of photons λ_i in each measurement is $N_i = N_{\text{ph}} \lambda_i / \sum_i \lambda_i$, and the corresponding rms shot noise is $\Delta N_i / N_i = \Delta \lambda_i / \lambda_i = 1 / \sqrt{N_i}$. We simulate the shot noise by adding a normally distributed random value with the rms deviation $\Delta \lambda_i$ to every λ_i .

We set N_{ph} to 100, 400, and 10,000 and add the photon shot noise numerically before training the DNNs. As can be seen from Fig. 7, the advantage of HGI over DI for $N_{\text{ph}} = 10^4$ is largely similar to the classical case. Particularly strong is the impact of the shot noise on the loss function of DI+DNN [Fig. 7(c)]: the neural network begins overfitting as early as at epoch 300.

On the other hand, the edge of HGI over DI+DNN degrades for $N_{\text{ph}} = 400$ and especially 100 [Fig. 8]. This is because the total number of photons available is no longer sufficient to reliably reconstruct the relatively intricate image even with the help of HGI.

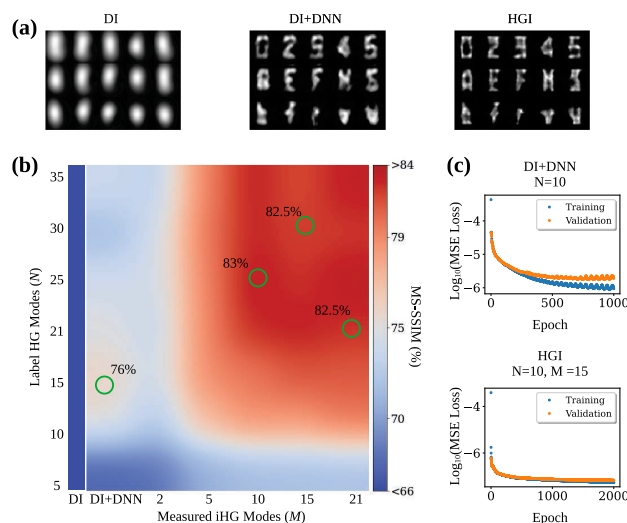


Fig. 7. (a) Alphabet letter images with simulated shot noise assuming $N_{ph} = 10000$ photons using DI (left), DNN-enhanced DI (middle), and HGI using $M = 15$ iHG modes (right). (b) MS-SSIM values for different pairs of inputs and labels. The performance is similar to the classical case. (c) Training and cross-validation MSE as a function of training epochs for selected input and label pairs. DI+DNN overfits at 300 epochs, at which point the training is stopped, while the DNN for HGI is trained for 2000 epochs.

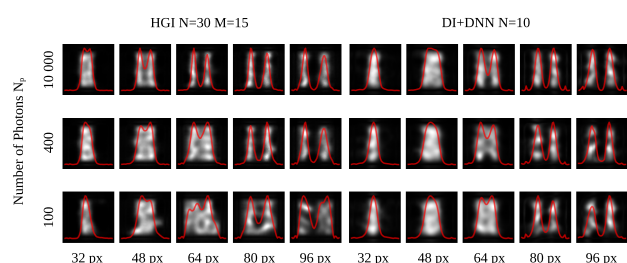


Fig. 8. Reconstructed images using HGI (left) and DI+DNN (right) of pairs of parallel lines with added photon shot noise for $N_{ph} = 100, 400, 10,000$.

5. CONCLUSION

Here we presented the first results in superresolving reconstruction of complex incoherent 2D objects by completely passive measurements using linear optics in the far-field regime. We have shown that a combination of information-rich measurements with a simple DNN produces images with ~ 3 -fold resolution improvement over DI. We can enhance the DI resolution by applying the same DNN; however, the resulting resolution is still a factor of ~ 2 below that achieved with HGI. This shows the key role of the new physics of HGI in resolution enhancement.

Due to its passive nature, HGI can become beneficial in various scenarios and has virtually no limitations on the samples that can be imaged. In microscopy, it could apply to samples that are easily damaged by near-field probes, possess no nonlinear properties, and/or can be affected by strong laser illumination. Additional interesting use cases are remote objects where active interaction with the sample is impossible altogether. Prime examples would be astronomy, precision agriculture, remote sensing, or satellite imaging.

The main obstacles to the practical application of our scheme are (1) the training of the DNN required for reconstruction and

(2) the shortcomings of heterodyne detection. For (1), the training set samples can be fabricated using commercially available fluorescent beads in various sizes. Alternatively, calibration slides can be fabricated with a resolution of a few tens of nanometers through lithography or laser writing. In both cases, the training samples will need to be imaged employing electron microscopy or another method to obtain ground truth data. With the rapid advancement of machine-learning technology, we can also envision that better DNN architectures and loss functions will emerge that would drastically reduce the size of the required training set. In the meantime, we can expand the training set using known data augmentation techniques [32].

For (2), we note that heterodyne detection is not optimal for HGI because of the shot noise of the powerful LO [33] and the necessity to measure the modes in a sequential manner, requiring a large photon budget. Moreover, heterodyning could not be directly applied to natural incoherent sources because of their broad linewidth. The optimal solution for measuring in the iHG basis is using a mode sorter, which spatially separates the iHG modes, after which their intensities can be measured by direct photodetection. The currently available mode sorters do not yet allow measuring higher-order modes in the visible spectrum, but the progress in this field is promising [34]. For heterodyne detection, improvement can be achieved with digital holography, i.e., measuring the interference pattern between the image field and a LO with a digital camera. This yields full information about the transverse distribution of the field amplitude and phase in the image plane and hence permits computing the fields in each iHG mode digitally [35,36]. This approach obviates sequential mode acquisition, but not the shot noise and linewidth issues. Regarding the latter point, incoherent holographic techniques might be a promising approach as they require no reference beam [37,38].

It would be interesting to combine HGI with existing passive SR microscopy methods based on engineered sample illumination, such as confocal and structured-illumination microscopy [39]. Because these methods and HGI rely on different physics to enhance resolution, we expect the enhancement effect achieved through both methods to be cumulative. In this way, we hope passive microscopy resolution with engineered illumination eventually reaches the scale of 50 nm.

Funding. H2020 Marie Skłodowska-Curie Actions (956071); Biotechnology and Biological Sciences Research Council (BB/X004317/1).

Disclosures. The authors declare no conflicts of interest.

Data availability. Data underlying the results presented in this paper are not publicly available at this time but may be obtained from the authors upon reasonable request.

Supplemental document. See Supplement 1 for supporting content.

REFERENCES

1. M. Yanoff and J. S. Duker, *Ophthalmology* (Elsevier Health Sciences, 2008).
2. L. Rayleigh, "XXXI. Investigations in optics, with special reference to the spectroscope," *London, Edinburgh, Dublin Philos. Mag. J. Sci.* **8**, 261–274 (1879).
3. E. Abbe, "Beiträge zur theorie des mikroskops und der mikroskopischen wahrnehmung," *Archiv für mikroskopische Anatomie* **9**, 413–468 (1873).
4. E. Abbe, "XV.—The relation of aperture and power in the microscope (continued)," *J. R. Microsc. Soc.* **3**, 790–812 (1883).
5. S. Pujals, N. Feiner-Gracia, P. Delcanale, I. Voets, and L. Albertazzi, "Super-resolution microscopy as a powerful tool to study complex synthetic materials," *Nat. Rev. Chem.* **3**, 68–84 (2019).

6. G. Huszka and M. A. Gijs, "Super-resolution optical imaging: a comparison," *Micro Nano Eng.* **2**, 7–28 (2019).
7. J. Valli, A. Garcia-Burgos, L. M. Rooney, B. V. de Melo e Oliveira, R. R. Duncan, and C. Rickman, "Seeing beyond the limit: a guide to choosing the right super-resolution microscopy technique," *J. Biol. Chem.* **297**, 100791 (2021).
8. S. Liu, P. Hoess, and J. Ries, "Super-resolution microscopy for structural cell biology," *Annu. Rev. Biophys.* **51**, 301–326 (2022).
9. L. Möckl, D. C. Lamb, and C. Bräuchle, "Super-resolved fluorescence microscopy: Nobel Prize in Chemistry 2014 for Eric Betzig, Stefan Hell, and William E. Moerner," *Angew. Chem. (Int. Ed.)* **53**, 13972–13977 (2014).
10. G. Binnig, C. F. Quate, and C. Gerber, "Atomic force microscope," *Phys. Rev. Lett.* **56**, 930 (1986).
11. D. Mathys, "Die Entwicklung der elektronenmikroskopie vom bild über die analyse zum nanolabor," in *Zentrum für Mikroskopie* (University of Basel, 2004), pp. 8.
12. M. Tsang, R. Nair, and X.-M. Lu, "Quantum theory of superresolution for two incoherent optical point sources," *Phys. Rev. X* **6**, 031033 (2016).
13. M. Tsang, "Subdiffraction incoherent optical imaging via spatial-mode demultiplexing," *New J. Phys.* **19**, 023054 (2017).
14. M. Tsang, "Resolving starlight: a quantum perspective," *Contemp. Phys.* **60**, 279–298 (2019).
15. M. Tsang and R. Nair, "Resurgence of Rayleigh's curse in the presence of partial coherence: comment," *Optica* **6**, 400–401 (2019).
16. M. Tsang, "Quantum limit to subdiffraction incoherent optical imaging," *Phys. Rev. A* **99**, 012305 (2019).
17. F. Yang, A. Tashchilina, E. S. Moiseev, C. Simon, and A. I. Lvovsky, "Far-field linear optical superresolution via heterodyne detection in a higher-order local oscillator mode," *Optica* **3**, 1148–1152 (2016).
18. Z. S. Tang, K. Durak, and A. Ling, "Fault-tolerant and finite-error localization for point emitters within the diffraction limit," *Opt. Express* **24**, 22004–22012 (2016).
19. M. Paúr, B. Stoklasa, Z. Hradil, L. L. Sánchez-Soto, and J. Rehacek, "Achieving the ultimate optical resolution," *Optica* **3**, 1144–1147 (2016).
20. W.-K. Tham, H. Ferretti, and A. M. Steinberg, "Beating Rayleigh's curse by imaging using phase information," *Phys. Rev. Lett.* **118**, 070801 (2017).
21. M. Parniak, S. Borówka, K. Boroszko, W. Wasilewski, K. Banaszek, and R. Demkowicz-Dobrzański, "Beating the Rayleigh limit using two-photon interference," *Phys. Rev. Lett.* **121**, 250503 (2018).
22. U. Zanforlin, C. Lupo, P. W. Connolly, P. Kok, G. S. Buller, and Z. Huang, "Optical quantum super-resolution imaging and hypothesis testing," *Nat. Commun.* **13**, 5373 (2022).
23. I. Ozer, M. R. Grace, and S. Guha, "Reconfigurable spatial-mode sorter for super-resolution imaging," in *Conference on Lasers and Electro-Optics (CLEO)* (IEEE, 2022), pp. 1–2.
24. A. Pushkina, G. Maltese, J. Costa-Filho, P. Patel, and A. Lvovsky, "Superresolution linear optical imaging in the far field," *Phys. Rev. Lett.* **127**, 253602 (2021).
25. B. Zhang, J. Zerubia, and J.-C. Olivo-Marin, "Gaussian approximations of fluorescence microscope point-spread function models," *Appl. Opt.* **46**, 1819–1829 (2007).
26. M. Tsang, "Subdiffraction incoherent optical imaging via spatial-mode demultiplexing: semiclassical treatment," *Phys. Rev. A* **97**, 023830 (2018).
27. W. H. Richardson, "Bayesian-based iterative method of image restoration," *J. Opt. Soc. Am. A* **62**, 55–59 (1972).
28. Z. Wang, E. Simoncelli, and A. Bovik, "Multiscale structural similarity for image quality assessment," in *The Thirty-Seventh Asilomar Conference on Signals, Systems & Computers* (2003), Vol. **2**, pp. 1398–1402.
29. H. Zhao, O. Gallo, I. Frosio, and J. Kautz, "Loss functions for image restoration with neural networks," *IEEE Trans. Comput. Imaging* **3**, 47–57 (2016).
30. E. Bolduc, N. Bent, E. Santamato, E. Karimi, and R. W. Boyd, "Exact solution to simultaneous intensity and phase encryption with a single phase-only hologram," *Opt. Lett.* **38**, 3546–3549 (2013).
31. A. Pushkina, J. Costa-Filho, G. Maltese, and A. Lvovsky, "Comprehensive model and performance optimization of phase-only spatial light modulators," *Meas. Sci. Technol.* **31**, 125202 (2020).
32. C. Shorten and T. M. Khoshgoftaar, "A survey on image data augmentation for deep learning," *J. Big Data* **6**, 1–48 (2019).
33. F. Yang, R. Nair, M. Tsang, C. Simon, and A. I. Lvovsky, "Fisher information for far-field linear optical superresolution via homodyne or heterodyne detection in a higher-order local oscillator mode," *Phys. Rev. A* **96**, 063829 (2017).
34. N. K. Fontaine, R. Ryf, H. Chen, D. T. Neilson, K. Kim, and J. Carpenter, "Laguerre-Gaussian mode sorter," *Nat. Commun.* **10**, 1865 (2019).
35. C. Zhou, J. Xin, Y. Li, and X.-M. Lu, "Measuring small displacements of an optical point source with digital holography," *Opt. Express* **31**, 19336–19346 (2023).
36. J. Rehacek, M. Paúr, B. Stoklasa, Z. Hradil, and L. L. Sanchez-Soto, "Optimal measurements for resolution beyond the Rayleigh limit," *Opt. Lett.* **42**, 231–234 (2017).
37. M. Kumar, O. Matoba, X. Quan, S. K. Rajput, Y. Awatsuji, and Y. Tamada, "Single-shot common-path off-axis digital holography: applications in bioimaging and optical metrology," *Appl. Opt.* **60**, A195–A204 (2021).
38. T. Tahara, "Review of incoherent digital holography: applications to multidimensional incoherent digital holographic microscopy and palm-sized digital holographic recorder—holosensor," *Front. Photon.* **2**, 829139 (2022).
39. K. K. Bearne, Y. Zhou, B. Braverman, J. Yang, S. Wadood, A. N. Jordan, A. Vamivakas, Z. Shi, and R. W. Boyd, "Confocal super-resolution microscopy based on a spatial mode sorter," *Opt. Express* **29**, 11784–11792 (2021).